Research Article Vol. 58, No. 6 / 20 February 2019 / Applied Optics 1393

applied optics

Wide-field off-axis telescope for the Mesospheric Airglow/Aerosol Tomography Spectroscopy satellite

Arvid Hammar,[1,2,*] Woojin Park,[3] Seunghyuk Chang,[4] Soojong Pak,[3] Anders Emrich,[1] and Jan Stake[2]

[1]Omnisys Instruments AB, August Barks gata 6B, SE-421 32 Västra Frölunda, Sweden
[2]Terahertz and Millimetre Wave Laboratory, Department of Microtechnology and Nanoscience—MC2, Chalmers University of Technology, SE-412 96 Gothenburg, Sweden
[3]School of Space Research, Kyung Hee University, 1732 Deokyoungdaero, Giheung-gu, Yongin-si, Gyeonggi-do 17104, South Korea
[4]Korea Advanced Institute of Science and Technology (KAIST), Center for Integrated Smart Sensors, Daejeon, South Korea
*Corresponding author: arvid.hammar@omnisys.se

Received 3 December 2018; revised 16 January 2019; accepted 16 January 2019; posted 17 January 2019 (Doc. ID 354436); published 14 February 2019

We present the development of a compact $f/7.3$ ($D = 35$ mm) three-mirror reflective telescope for the atmospheric-research microsatellite Mesospheric Airglow/Aerosol Tomography Spectroscopy (MATS). The telescope design was driven by the end users' need for a reflective wide-field (5.67° × 0.91°) optic with high stray light rejection and six detection channels with separate image sensors, operating at wavelengths 270–772 nm. For the first time, a design method for wide-field off-axis telescopes—in which linear astigmatism is eliminated—was applied and tested in practice. Single-point diamond turning was used to produce two sets of 37–110 mm large free-form aluminum mirrors with surface figure errors and roughness values of 34–62 nm (RMS)/193–497 nm (PV) and 2.8–3.5 nm (RMS), respectively. A method that combines precise machining and geometry measurements (using a coordinate measuring machine) was employed to fabricate an aluminum structure to accurately position the mirrors without the need for manual alignment. The telescope was tested with a network of plate beamsplitters and filters, which define the spectral selection for the six detection channels. Imaging performance measurements were carried out using a reflective off-axis collimator, which projects imaging targets at infinite focus. A modulation transfer function (MTF) value of 0.45 at 20 lp/mm was measured at ∼760 nm (diffraction limit: 0.85) using a slanted edge target. By modeling the measured mirror surfaces in optical design software, a reoptimization of the mirror positions could be performed and an improved MTF of ∼0.75 at 20 lp/mm was predicted. The results demonstrate design- and building methods that can be utilized to make off-axis telescopes for a vast range of applications.

https://doi.org/10.1364/AO.58.001393

1. INTRODUCTION

At altitudes between 70 and 110 km, where the mesosphere transitions into the mesopause/thermosphere, ascending large-scale air pressure waves expand rapidly and break apart due to decreased atmospheric pressure. These are called gravity waves (not to be confused with gravitational waves) and act as a driver of midatmospheric circulation, which transfers heat and momentum between the various layers of the atmosphere [1]. Gravity waves therefore play an important role in the overall dynamics of the atmosphere and should be investigated for improved climate modeling and weather prediction [2]. Several satellite-borne instruments have therefore been used in recent years to study gravity waves [3–6]. However, there is currently a lack of measurement data for gravity waves with wavelengths below 20 km vertically and 100 km horizontally [7]. This has motivated the development of a new satellite-borne low Earth orbit instrument called Mesospheric Airglow/Aerosol Tomography Spectroscopy (MATS) [8], which is scheduled for launch in late 2019.

MATS will use four optical instruments to collect measurement data, whereof the main one is directed toward the atmospheric limb and the three others point in the nadir direction. The limb instrument will have six channels to study gravity waves through emissions from O_2 atmospheric airglow (NIR, 759–767 nm) [9] and noctilucent clouds (UV, 270–304.5 nm) [10]. Combining multiple images taken from different directions and from different wavelength bands, spectroscopy and tomographic methods can be used to obtain three-dimensional wave patterns and temperature distributions in the mesosphere [11,12].

To resolve both small- and large-scale gravity waves at UV and NIR wavelengths, a reflective telescope design with a relatively large field of view (FoV) is needed for the limb instrument. On-axis telescope designs with three mirrors and that are corrected for the main third-order aberrations (i.e., spherical aberration, coma, astigmatism, and field curvature) are often referred to as three-mirror anastigmats (TMAs) [13]. These have therefore found several applications throughout the years [14–16]. However, strict stray light requirements associated with the mission [17] and the need for efficient accommodation of the six detection channels called for an off-axis design of the limb instrument. Off-axis versions of TMAs have gained popularity [18–22], in part due to developments in mirror manufacturing where fully free-form metallic surfaces can be made using high-precision single-point diamond turning (SPDT) [23,24]. Unlike on-axis systems, the dominating aberration for off-axis telescopes is the lower-order linear astigmatism [25], which introduces a relative tilt between the tangential and sagittal image planes. Unless corrected for, linear astigmatism will limit the performance for large FoV off-axis telescopes.

Using the closed-form analytical expressions to remove linear astigmatism [26], an off-axis three-mirror telescope with six separate image planes was designed for the MATS limb instrument. Two sets of telescope mirrors were manufactured using SPDT, which resulted in excellent surface figures. The mirrors were mounted in high-precision aluminum structures, which were part of the breadboard and prototype models used for imaging performance tests. This is the first time a telescope design based on the method of elimination of linear astigmatism is built and tested. With relatively modest imaging requirements for the limb instrument, it was possible to manufacture the mounting structures with high accuracy so that the mirrors could be mounted without the need for manual alignment.

2. PAYLOAD OVERVIEW

MATS is the first instrument to use the InnoSat microsatellite platform [27], which will be the basis for a new program of small satellites that use the same standard platform. The 50 kg platform can support payloads of 65 cm × 53 cm × 48 cm in size and masses up to 20 kg–see Fig. 1. MATS will be launched into a sun-synchronous low Earth orbit (585 km altitude), which enables the use of a single solar panel and temperature regulation using passive radiative coolers and resistive heaters.

The $f/7.3$ telescope of the limb instrument uses a 35 mm entrance pupil diameter to capture a 250 km × 40 km atmospheric scene at a distance of ∼2600 km, which leads to a FoV of 5.67° × 0.91°. To measure gravity wave structures with features down to 200 m, the limb telescope must have an MTF of at least 0.5 at 20 lp/mm in the vertical direction (c.f. Table 1). Horizontally, the imaging requirements are much less strict since only structures in the order of 5–50 km must be resolved. Back-illuminated CCD image sensors with a resolution of 515 × 2048 (6.9 mm × 27.6 mm) will be used for all channels [28]. On-chip binning will be used, which results in a maximum Nyquist frequency of 18.6 lp/mm.

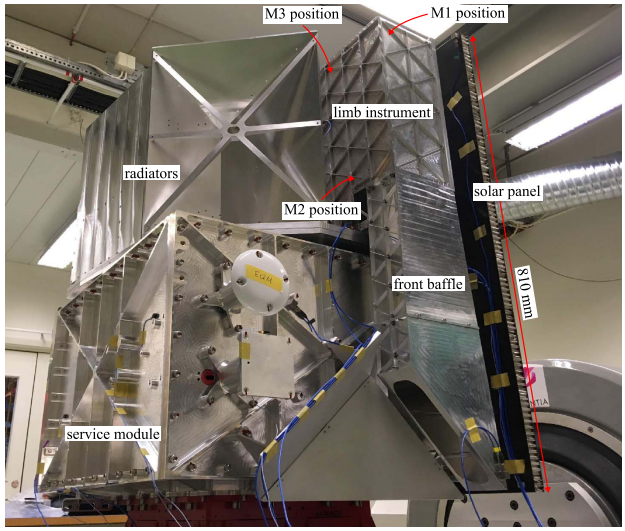

Fig. 1. Structural model of MATS mounted on the InnoSat platform for vibration tests.

Table 1. Wavelength Bands (λ) and Vertical Resolution Requirements (ν) of the Limb Telescope, Where the Latter Are Given in Terms of Spatial Resolution, Where MTF = 0.5

Channel	λ(nm)	ν (lp/mm)
UV1	270.0 ± 1.5	20.0
UV2	304.5 ± 1.5	20.0
IR1	762.0 ± 1.8	10.0
IR2	763.0 ± 4.0	10.0
IR3	754.0 ± 1.5	5.0
IR4	772.0 ± 1.5	5.0

3. OPTICAL DESIGN

The basic optical layout of the telescope was designed to fit within the payload volume of the satellite platform while accommodating all six imaging channels. By choosing a relatively long back focal length of ∼450 mm, a network of beamsplitters, filters, folding mirrors, and image sensors of the limb instrument could be accommodated. The full implementation of the telescope with its six channels is shown in Fig. 2. The thicknesses and tilts of the instrument's glass components were chosen so that the optical path length became identical for all channels (The initial design included three pellicle beamsplitters for the IR1–4 channels. However, tests later revealed that the reflected wavefront error became too big, and, hence, these components were replaced by plate beamsplitters—see Section 5). Broadband filters remove visible light, whereas the final spectral selections are defined by narrowband filters placed in front of each image sensor.

A starting point for the telescope design was obtained by employing a method in which three confocal mirrors fulfilled the condition to eliminate linear astigmatism [26]:

$$(1+m_1)m_2m_3\tan i_1+(1+m_2)m_3\tan i_2+(1+m_3)\tan i_3=0. \quad (1)$$

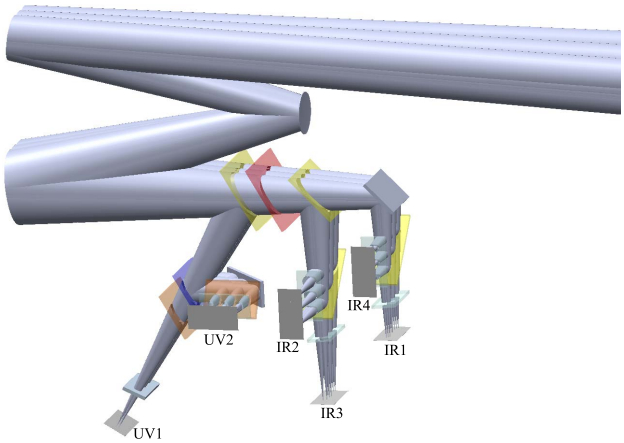

Fig. 2. Limb telescope with the network of beamsplitters, filters, folding mirrors, and image sensors. Beamsplitters are shown in yellow/blue, broadband filters in red/orange, and narrowband filters in light blue.

Here, $m_{1\text{-}3}$ and $i_{1\text{-}3}$ denote mirror magnifications and corresponding optical-axis ray reflection angles, respectively. Table 2 and Fig. 3 summarize the geometry for the basic telescope design. The aperture stop was placed on the secondary M2 mirror, which is situated at approximately equal distances from M1 and M3, which in turn act to restrict the size of these apertures. The relatively long back-focal length results in nearly identical angles of incidence when light from across the FoV hits the narrowband interference filters. This makes shifts in the central wavelengths of the filters insignificant and ensures a correct spectral selection across each captured image.

Table 2. Inter-Mirror Distances, Optical-Axis Ray Reflection Angles, and Mirror Magnifications of the Basic Telescope Design

Parameter	Value	Unit
M1–M2	250.00000	mm
M2–M3	247.45000	mm
M3–focal plane	453.62630	mm
i_1	−6.00000	°
i_2	15.00000	°
i_3	−8.18937	°
m_1	0.00000	–
m_2	0.19482	–
m_3	0.92393	–

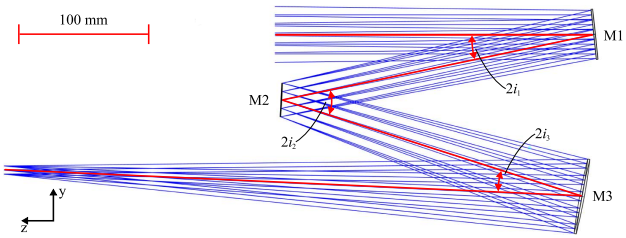

Fig. 3. Basic three-mirror off-axis design for the limb telescope. The optical-axis ray is shown in red.

The surface sag z of each mirror was defined by the following polynomial:

$$z(x,y) = \sum_{i=1}^{45} A_i E_i(x,y), \tag{2}$$

where A_i are real coefficients and $E_1 = x, E_2 = y, E_3 = x^2, E_4 = xy, E_5 = y^2, \ldots E_{43} = x^2y^6, E_{44} = xy^7$, and $E_{45} = y^8$. To impose symmetry in the yz-plane, all coefficients A_i with odd powers of x were set to zero. Implementing the design in Zemax Opticstudio and optimizing the coefficients for the mirror surfaces, intermirror distances and mirror tilts resulted in a design with diffraction-limited performance over a FoV of 13.8° × 4.0° at 270 nm. However, this requires larger M1 and M3 mirrors than the ones used in the design, which were made to match the required FoV of 5.67° × 0.91° without vignetting. Obstruction of the mirrors in the vertical direction limits the maximum vertical FoV for the design (c.f. Fig. 3). Slightly oversized masking apertures were used in front of the CCDs to block unwanted light. To correct for wavefront errors introduced by the network of filters and beamsplitters, three 3 mm glass plates were inserted into the optical path before performing a final optimization of the design where intermirror distances, reflection angles, and mirror surfaces were fine-tuned.

A basic tolerance analysis was performed to identify sensitive parts of the telescope and to get an indication of overall mirror alignment requirements. Mirrors were first tilted and moved in-plane individually, and so were the two intermirror distances. Focus compensation was used in all cases. Acceptable tilt errors of the mirrors about the x and y axis (c.f. Fig. 3) were in the range 0.05°–0.4°. Tilt errors around the x axis for M1 and y axis for M3 were the most sensitive, 0.05° and 0.1°, respectively. The system was particularly insensitive to in-plane translations of the mirrors. No major degradation of the imaging quality for translations up to 500 μm were seen. For the intermirror separations, the results showed individual errors up to 500 μm were tolerable. However, larger errors required focus compensations up to 2 mm, which is more than the mechanical implementation allows for—see Section 4. A Monte Carlo analysis was also performed, which showed that overall tolerances of: 100 μ should be acceptable.

4. OPTOMECHANICAL DESIGN AND PROTOTYPING

Manufacturing of the mirrors began with CNC machining of the blanks made of 6061 T6 rapidly solidified aluminum. This step determined the overall geometry while leaving some material to be removed in the subsequent SPDT process, which defined the final mirror surfaces. Before removing each mirror from the workholder of the SPDT machine, the three mounting interfaces were made using the same cutting tool, providing an offset error less than 300 nm to the mirror surface. Hence, the mounting interfaces could later be used as reference surfaces when aligning the mirrors. Thermal expansion zones were defined around each mounting interface to avoid warping the mirrors due to changed temperature conditions—see Figs. 4 and 6.

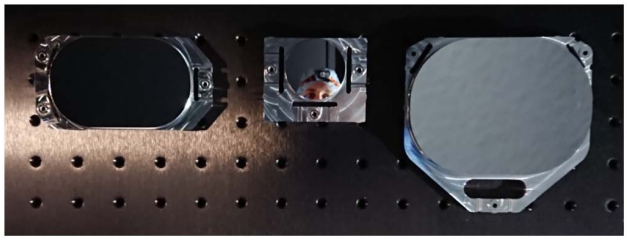

Fig. 4. Prototype freeform mirrors. From left to right: M1, M2, and M3.

Coating the mirrors with NiP and subsequent polishing can reduce the surface roughness down to 0.6 nm and lead to a two-orders-of-magnitude reduction of nonspecular reflections [29]. However, to avoid excess surface deformation due to the mismatch in thermal expansion coefficients between aluminum and NiP, a protective aluminum coating with no polishing was used instead.

The first set of manufactured mirrors was used for breadboard and prototype tests. The surface errors were measured using a tactile method, and the results were taken as input to improve the surface figures of the second set of mirrors, which are intended for flight. Figure 5 and Table 3 summarize large-scale surface errors and surface roughness for the breadboard/prototype and flight mirrors.

With six degrees of freedom for each of the three mirrors, alignment with manual tuning of tilts can be a difficult process that may require interferometric and computer-aided

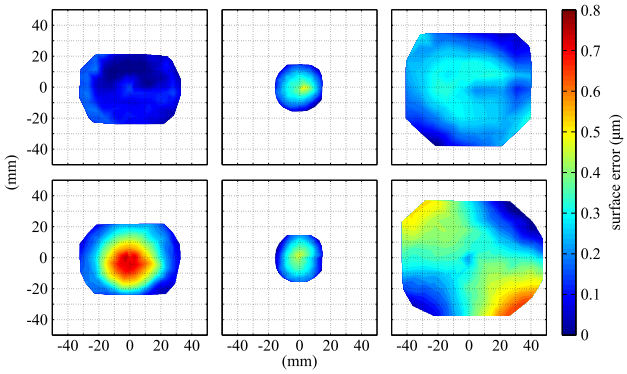

Fig. 5. Measured surface errors of the flight mirrors (top row) and prototype mirrors (bottom row). From left to right: M1, M2, and M3.

Table 3. Measured Surface Figure Error (PV/RMS) and Surface Roughness (PV/RMS) of SPDT Flight and Prototype Mirrors

Mirror	Error (nm)	Roughness (nm)
M1 flight	193/49	23.5/2.9
M1 prototype	799/61	55.0/2.6
M2 flight	497/34	20.5/3.3
M2 prototype	456/42	30.0/2.2
M3 flight.	340/62	24.5/3.5
M3 prototype	674/143	34.0/3.0

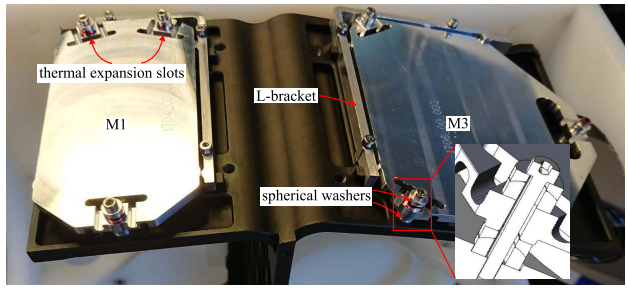

Fig. 6. M1 and M3 breadboard/prototype mirrors fixed in the black-coated aluminum mounting structure. A cross section of a mounting point with spherical washers on each side of the mirror is shown at the bottom.

techniques [19]. Therefore, an approach where the mirror positions were defined by six mating interfaces to a high-precision mounting structure was used instead [30].

The breadboard mounting structure was milled from a single block of aluminum, which had tolerances in the order 50–100 μm (measured using a coordinate measuring machine) and hence within predicted tolerances (c.f. Section 3). As shown in Fig. 6, spherical washers were used to interface between the mounting structure and the mirrors. The thickness of these washers uniquely determine the tilt of the mirrors and was machined to compensate for the measured errors of the breadboard mounting structure but not surface figure errors of the prototype mirrors. Moreover, this scheme also ensures minimization of stresses in the mirrors when these are fixed to the mounting structure. Lateral offsets of the mirrors were controlled in the same manner using L-shaped brackets (cf. Fig. 6).

The breadboard setup was based on an optical table where the mirror mounting structure was simply placed behind a beamsplitter, followed by a broadband filter and a narrowband filter to achieve the intended imaging performance. This setup was fully representative in terms of optical resolution but could only be used to test one imaging channel at the time. However, with full adjustability of the CCD image sensor, this setup could be used as a benchmark for the optical performance of the limb telescope. The prototype model was a highly flight-representative and had beamsplitters and filters for all six imaging channels—see Fig. 7. A main housing for the entire

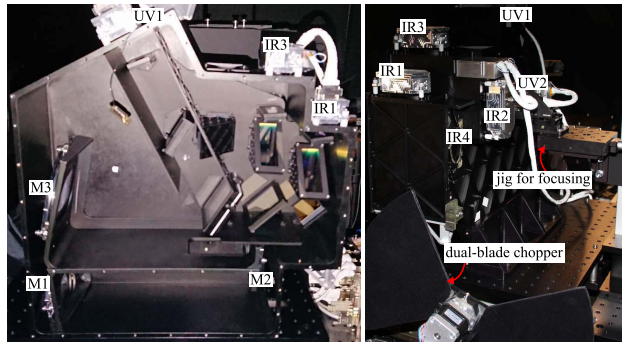

Fig. 7. Limb instrument prototype in the optics test bench. The side cover was taken for the illustrative purposes in the left image. The dual-blade chopper used as shutter and a jig with micrometer stages used for focusing are also shown in the right image.

optical chain was milled from a single block of aluminum and coated with black nickel. The six CCD sensors were mounted on the outside of the housing using standoffs made from a glass-ceramic (Macor) to achieve thermal decoupling. This setup allowed for no manual adjustment of the optical components, except for the CCD sensors that could be moved ±2 mm for focusing.

5. IMAGING PERFORMANCE

A reflective collimator based on an off-axis parabolic mirror was used for the optical tests of the limb telescope. The collimator had a 110 mm aluminum-coated parabolic mirror ($f/9$) with a resolution better than 80 lp/mm and a FoV of 3.3°. A 150 W Xe source and a diffuser were used to accomplish a uniform illumination of the focal-plane imaging targets, which were mounted on a rotary wheel. It was unfortunately discovered that the diffusor had an incorrect coating with high absorption below 400 nm. With virtually no output power in the UV bands at time of testing, it was only possible to test the imaging performance at NIR wavelengths. The targets used for tests were a 1951 USAF resolution test chart, an edge target (for MTF measurements), and various pinhole targets. Since the collimator could not cover the entire FoV, the optic was mounted on a rotary stage with the axis of rotation coinciding with the center of M1 to enable sweeping in the horizontal direction. A dual-blade chopper was placed in front of M1 and used as a shutter to define the exposure time. Although the flight system will not include a shutter, it was deemed preferable during testing since the effect of read-out smearing could be removed without any postprocessing of the measured data.

The initial measurements were performed in a breadboard configuration with the telescope mounted on an optical bench and with full adjustability of the CCD sensor. As part of the initial design, three rectangular pellicle beamsplitters were used in the optical path for the four NIR channels (cf. Fig. 2) to achieve identical optical path length for all six channels of the instrument and to minimize potential ghosting problems. However, since uneven strain in the membrane of the rectangular pellicle beamsplitters were known a priori to create excess curvature, the two solutions were compared experimentally. The results are summarized in Figs. 8 and 9. As can be seen, the pellicle beamsplitter in the reflective mode leads to a substantial decrease in resolution compared to a 3 mm plate beamsplitter in the transmission mode. Hence, the latter solution was chosen for the prototype and upcoming flight model. By placing the IR1 and IR2 channels at the positions with the highest resolution (predicted from simulations), the resolution requirements (c.f. Table 1) for all channels could still be fulfilled.

A number of issues were revealed when performing tests with the full limb instrument prototype. Most notably, late discovered manufacturing errors led to decreased tolerances for the mirror mounting structure, which in turn resulted in worsened imaging performance that was not corrected for. This most likely happened because of an incorrectly performed thermal stress relief. Generally, the measured MTF from the prototype was in the order of 0.1 at 20 lp/mm and thus below the required value of 0.5. In addition, an excessive misalignment between channels could be attributed to incorrectly mounted beamsplitters/filters, which caused tilt errors. Nevertheless, the prototype test campaign still offered an opportunity to test building concepts and focusing procedures for the upcoming flight model. The latter was performed using custom jigs for each channel (see Fig. 7), where the CCDs could be moved along the optical axis with respect to the limb house (c.f. Fig. 7). Figure 10 shows a compilation of (scaled up) point-source images taken with the prototype.

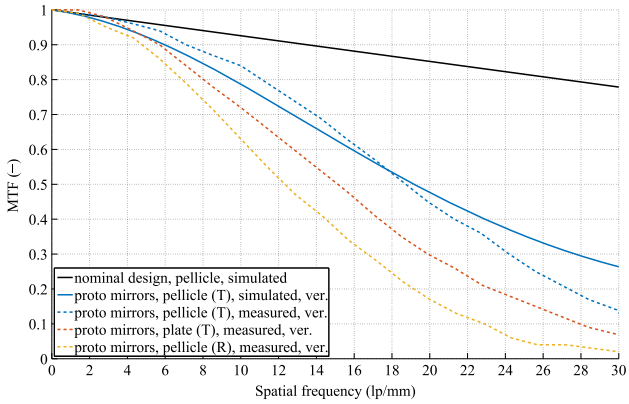

Fig. 8. Measured MTF curves in the NIR (IR2) of the telescope breadboard at the center of its FoV. Transmission/reflection in the pellicle beamsplitter is compared to transmission through a 3 mm plate beamsplitter. The simulated MTF data was obtained using measured prototype mirror surfaces and was averaged over different field points across the FoV.

The measured surface errors of the mirror were largely symmetric (c.f. Fig. 5), which primarily alters the focal lengths. This implies that the condition to eliminate linear astigmatism

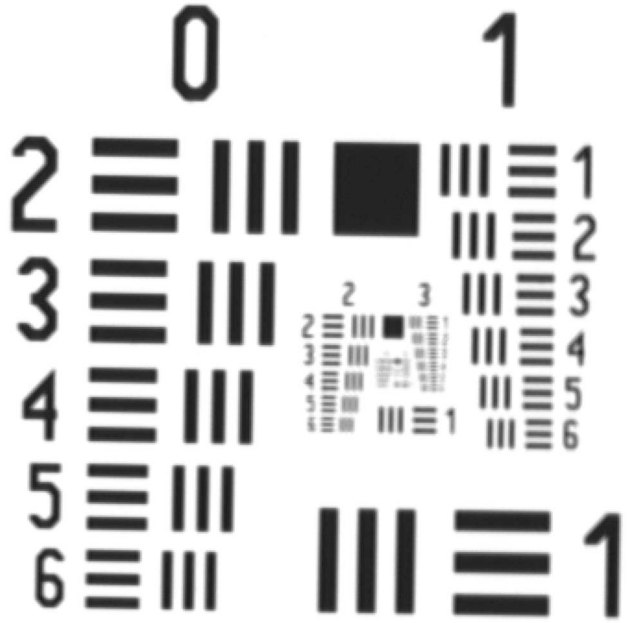

Fig. 9. Image of a USAF 1951 test chart taken by the MATS breadboard telescope with an IR2 narrowband filter, a pellicle beamsplitter in the transmission mode, and a CCD image sensor with 13 μm pixels.

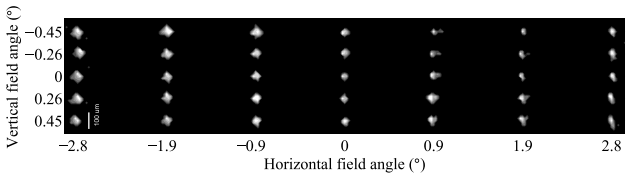

Fig. 10. Point source measurement across the entire FoV of the limb instrument prototype. Note that the image size of each point source has been scaled up for illustrative purposes.

[Eq. (1)] is not fulfilled, and the wide-field performance of the telescope consequently degrades. It was therefore decided to investigate if the resolution could be improved for the flight model by optimizing the mirror positions using the measured surface figures. With the same basis functions used to describe the ideal surfaces [Eq. (2)], polynomials for the measured mirrors (prototype and flight) could be obtained through an iterative fitting process. A maximum residual error (PV) between the measured and fitted surfaces of 120 nm was obtained. The peak error typically occurred in the center of each mirror, corresponding to the axis of rotation during the SPDT machining.

The fitted mirror surfaces were implemented in Zemax Opticstudio, where the mirror positions were optimized for minimized RMS spot diameter across the FoV. Eight different setups were investigated, corresponding to all possible combinations of prototype and flight mirrors. As the limb instrument prototype housing (c.f. Fig. 7) will be reused for flight, a number of constraints were imposed to the optimization since the positions of beamsplitters, filters, and CCD sensors are defined by the housing geometry and thus fixed. The tilt angles i_1, i_2 [c.f. Eq. (1)] and the M1–M2 distance were taken as variables, whereas i_3 and the M2–M3 and M3–beamsplitter distances were calculated analytically from the geometrical constraints for each set of variable values. Minor in-plane (<100 μm) adjustments of the mirrors were applied in the last step of the optimization to compensate for the small offsets between the midpoint of the mirrors and the reference surfaces on the sides.

A set of predicted MTF curves across the FoV for the breadboard configuration is shown in Fig. 11. By running the optimization for all eight possible combination of prototype and flight mirrors, it was concluded that the flight mirrors were indeed able to produce the best imaging performance. However, nearly equal performance was obtained by replacing the flight M3 with its prototype counterpart. As can be seen in Fig. 11, a significant increase of the MTF can be expected using the flight mirror positions optimized for the measured surface errors. An average MTF of 0.75 is predicted at 20 lp/mm in the NIR, while the corresponding number is 0.81 in UV (not shown in Fig. 11).

For the particular optimized solution that was found, the x-axis tilts for M1, M2, and M3 were adjusted by 0.22°, 0.27°, and 0.04°, respectively. Intermirror distances changed by 6.36 and 3.33 mm, which ensured keeping the focus compensation of the CCD within 2 mm.

6. CONCLUSION

A reflective off-axis three-mirror telescope for the MATS limb instrument has been designed, built, and tested. The design

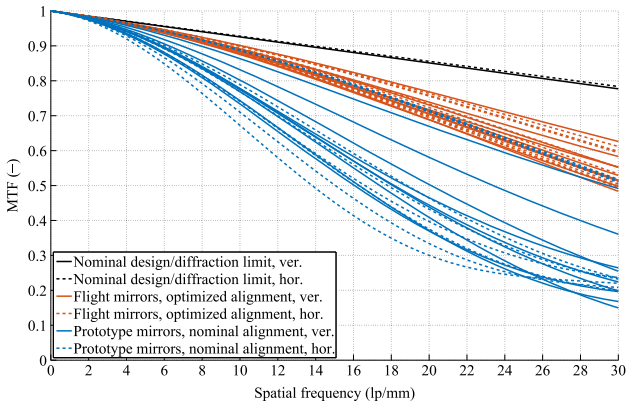

Fig. 11. Simulated MTF curves for the IR2 channel of the limb telescope over the nominal FoV for flight mirrors with optimized alignment and prototype mirrors with nominal alignment. Vertical (tangential) and horizontal (sagittal) fields are indicated with solid and dashed lines, respectively.

achieved diffraction-limited performance over a FoV of 13.8° × 4.0° at 270 nm by employing a design method to eliminate linear astigmatism, which (unless corrected for) becomes the major limiting aberration for off-axis wide-field telescopes. Two sets of aluminum mirrors were machined using a high-precision SPDT process. Measured surface figure errors and roughness values were 34–62 nm (RMS)/193–497 nm (PV) and 2.8–3.5 nm (RMS), respectively. A telescope breadboard model and a highly flight-representative prototype of the MATS limb instrument were built. With accurate positioning of the mirrors, measurements revealed MTF values of 0.45 at 20 lp/mm at wavelengths of approximately 760 nm. This is the first time that a telescope design based on the elimination of linear astigmatism has been built and tested. Tolerance problems detected in the prototype model motivated an investigation on how to improve the optical resolution for the flight model. By implementing the measured surface errors of the six manufactured mirrors into Zemax Opticstudio, alignment for different flight/prototype mirror configurations could be investigated. The simulated results show that the mirrors intended for flight indeed provide the best imaging performance, which is predicted to be 0.75 at 20 lp/mm and a wavelength of 763 nm. In summary, this work has presented efficient design and building methods that are highly applicable, even outside the field of space-borne Earth observation.

Funding. The MATS satellite is funded by the Swedish National Space Agency (SNSA). The development of off-axis telescopes was supported by the National Research Foundation of Korea (NRF) (NRF-2014M1A3A3A02034810; BK21 plus).

Acknowledgment. The authors are thankful to the staff at Millpond Optics for providing excellent results for the SPDT mirrors.

REFERENCES

1. D. C. Fritts and M. J. Alexander, "Gravity wave dynamics and effects in the middle atmosphere," Rev. Geophys. **41**, 247–265 (2003).
2. R. A. Akmaev, "Whole atmosphere modeling: connecting terrestrial and space weather," Rev. Geophys. **49**, RG4004 (2011).

3. M. Krebsbach and P. Preusse, "Spectral analysis of gravity wave activity in SABER temperature data," Geophys. Res. Lett. **34**, L03814 (2007).
4. H. Fischer, M. Birk, C. Blom, B. Carli, M. Carlotti, T. von Clarmann, L. Delbouille, A. Dudhia, D. Ehhalt, M. Endemann, J. M. Flaud, R. Gessner, A. Kleinert, R. Koopman, J. Langen, M. López-Puertas, P. Mosner, H. Nett, H. Oelhaf, G. Perron, J. Remedios, M. Ridolfi, G. Stiller, and R. Zander, "MIPAS: an instrument for atmospheric and climate research," Atmos. Chem. Phys. **8**, 2151–2188 (2008).
5. C. von Savigny, C. Robert, H. Bovensmann, J. P. Burrows, and M. Schwartz, "Satellite observations of the quasi 5-day wave in noctilucent clouds and mesopause temperatures," Geophys. Res. Lett. **34**, L24808 (2007).
6. V. Limpasuvan, D. L. Wu, M. J. Schwartz, J. W. Waters, Q. Wu, and T. L. Killeen, "The two-day wave in EOS MLS temperature and wind measurements during 2004–2005 winter," Geophys. Res. Lett. **32**, L17809 (2005).
7. P. Preusse, S. D. Eckermann, and M. Ern, "Transparency of the atmosphere to short horizontal wavelength gravity waves," J. Geophys. Res. **113**, D24104 (2008).
8. N. Larsson, R. Lilja, J. Gumbel, O. M. Christensen, and M. Örth, "The MATS micro satellite mission—tomographic perspective on the mesosphere," in *4s Symposium* (ESA Conference Bureau, 2016), pp. 11070–11078.
9. M. G. Mlynczak and D. S. Olander, "On the utility of the molecular oxygen dayglow emissions as proxies for middle atmospheric ozone," Geophys. Res. Lett. **22**, 1377–1380 (1995).
10. M. Gadsden and W. Schröder, *Noctilucent Clouds* (Springer, 1989), pp. 1–12.
11. O. M. Christensen, P. Eriksson, J. Urban, D. Murtagh, K. Hultgren, and J. Gumbel, "Tomographic retrieval of water vapour and temperature around polar mesospheric clouds using Odin-SMR," Atmos. Meas. Tech. **8**, 1981–1999 (2015).
12. E. Llewellyn, N. Lloyd, D. Degenstein, R. Gattinger, S. Petelina, A. Bourassa, J. Wiensz, E. Ivanov, I. McDade, and B. Solheim, "The OSIRIS instrument on the Odin spacecraft," Can. J. Phys. **82**, 411–422 (2004).
13. D. Korsch, "Closed form solution for three-mirror telescopes, corrected for spherical aberration, coma, astigmatism, and field curvature," Appl. Opt. **11**, 2986–2987 (1972).
14. R. Willstrop, "The Mersenne–Schmidt: a three-mirror survey telescope," Mon. Not. R. Astron. Soc. **210**, 597–609 (1984).
15. J. Nella, P. D. Atcheson, C. B. Atkinson, D. Au, A. J. Bronowicki, E. Bujanda, A. Cohen, D. Davies, P. A. Lightsey, R. Lynch, R. Lundquist, M. T. Menzel, M. Mohan, J. Pohner, P. Reynolds, H. Rivera, S. C. Texter, D. V. Shuckstes, D. D. Fitzgerald Simmons, R. C. Smith, P. C. Sullivan, D. D. Waldie, and R. Woods, "James Webb Space Telescope (JWST) observatory architecture and performance," Proc. SPIE **5487**, 576–587 (2004).
16. R. Laureijs, J. Amiaux, S. Arduini, J.-L. Augueres, J. Brinchmann, R. Cole, M. Cropper, C. Dabin, L. Duvet, and A. Ealet, "Euclid definition study report," arXiv:1110.3193 (2011).
17. A. Hammar, O. M. Christensen, W. Park, S. Pak, A. Emrich, and J. Stake, "Stray light suppression of a compact off-axis telescope for a satellite-borne instrument for atmospheric research," Proc. SPIE **10815**, 108150F (2018).
18. L. Wei, L. Zhang, X. Gong, and D.-M. Ma, "Design and optimization for main support structure of a large-area off-axis three-mirror space camera," Appl. Opt. **56**, 1094–1100 (2017).
19. M. P. Chrisp, B. Primeau, and M. A. Echter, "Imaging freeform optical systems designed with NURBS surfaces," Opt. Eng. **55**, 071208 (2016).
20. S. Grabarnik, M. Taccola, L. Maresi, V. Moreau, L. de Vos, J. Versluys, and G. Gubbels, "Compact multispectral and hyperspectral imagers based on a wide field of view TMA," Proc. SPIE **10565**, 1056505 (2017).
21. D. C. Reuter, S. A. Stern, J. Scherrer, D. E. Jennings, J. W. Baer, J. Hanley, L. Hardaway, A. Lunsford, S. McMuldroch, and J. Moore, "Ralph: a visible/infrared imager for the New Horizons Pluto/Kuiper Belt mission," Space Sci. Rev. **140**, 129–154 (2008).
22. S. G. Ungar, J. S. Pearlman, J. A. Mendenhall, and D. Reuter, "Overview of the earth observing one (EO-1) mission," IEEE Trans. Geosci. Remote Sens. **41**, 1149–1159 (2003).
23. R. Steinkopf, A. Gebhardt, S. Scheiding, M. Rohde, O. Stenzel, S. Gliech, V. Giggel, H. Löscher, G. Ullrich, and P. Rucks, "Metal mirrors with excellent figure and roughness," Proc. SPIE **7102**, 71020C (2008).
24. S. Risse, A. Gebhardt, C. Damm, T. Peschel, W. Stökl, T. Feigl, S. Kirschstein, R. E. N. Kaiser, and A. Tünnermann, "Novel TMA telescope based on ultra precise metal mirrors," Proc. SPIE **7010**, 701016 (2008).
25. S. Chang and A. Prata, "Geometrical theory of aberrations near the axis in classical off-axis reflecting telescopes," J. Opt. Soc. Am. A **22**, 2454–2464 (2005).
26. S. Chang, "Linear astigmatism of confocal off-axis reflective imaging systems with n-conic mirrors and its elimination," J. Opt. Soc. Am. A **32**, 852–859 (2015).
27. OHB Sweden, "MATS/InnoSat," 2019, http://www.ohb-sweden.se/space-missions/mats-innosat/.
28. G. Giono, G. Olentšenko, N. Ivchenko, O. M. Christensen, J. Gumbel, U. Frisk, A. Hammar, I. Davies, and L. Megner, "Characterisation of the analogue read-out chain for the CCDs onboard the mesospheric airglow/aerosol tomography and spectroscopy (MATS)," Proc. SPIE **10698**, 106984Y (2018).
29. R.-R. Rohloff, A. Gebhardt, V. Schönherr, S. Risse, J. Kinast, S. Scheiding, and T. Peschel, "A novel athermal approach for high-performance cryogenic metal optics," Proc. SPIE **7739**, 77394E (2010).
30. R. B. Johnson, "Wide field of view three-mirror telescopes having a common optical axis," Opt. Eng. **27**, 121046 (1988).